Topologically Tunable Polaritons Based on a Two-Dimensional Crystal in a Photonic Lattice

L. Lackner,[1] O. A. Egorov,[2] A. Ernzerhof,[1] C. Bennenhei,[1] V. N. Mitryakhin,[1] G. Leibeling,[3] F. Eilenberger,[3,4] S. Tongay,[5] U. Peschel,[2] M. Esmann,[1] and C. Schneider[1]

[1]*Institut für Physik, Fakultät V, Carl von Ossietzky Universität Oldenburg, 26129 Oldenburg, Germany*
[2]*Institute of Condensed Matter Theory and Optics, Friedrich Schiller University, 07745 Jena, Germany*
[3]*Fraunhofer-Institute for Applied Optics and Precision Engineering IOF, 07745 Jena, Germany*
[4]*Institute of Applied Physics, Abbe Center of Photonics, Friedrich Schiller University, 07745 Jena, Germany*
[5]*Materials Science and Engineering, School for Engineering of Matter, Transport, and Energy, Arizona State University, Tempe, Arizona 85287, USA*

(Received 5 June 2024; revised 7 April 2025; accepted 10 September 2025; published 15 October 2025)

Structured optical cavities have advanced as a powerful test bed to study lattice Hamiltonians in general, and topological phenomena in particular. The *in situ* tuning of topological modes, enabled via substantial modifications of emulated lattice potentials, has remained out of experimental reach due to the commonly utilized monolithic cavity samples. Here, we study the Su-Schrieffer-Heeger (SSH) lattice Hamiltonian, which we emulate in a widely tunable open optical cavity strongly coupled to excitons in an integrated WS_2 monolayer. The potential landscape comprises a topological domain boundary hosting a topological, exponentially localized mode at the interface between two lattices characterized by different Zak phases. The mode is spectrally tunable over 80 meV. Moreover, we use the unique tilt tunability of our implementation to transform the SSH lattice into a Stark ladder. This transformation couples the topologically protected defect mode to propagating lattice modes and effectively changes the symmetry of the system. Furthermore, it allows us to directly quantify the Zak-phase difference $\Delta_{Zak} = (1.07 \pm 0.11)\pi$ between the two topological phases. Our Letter constitutes an important step toward *in situ* tuning topological lattices to control and guide light on nonlinear chips.

DOI: 10.1103/qphl-qd37

Beyond the study of fundamental aspects of light-matter coupling and in nonlinear photonics, exciton polaritons are considered one of the prime experimental platforms in the field of topological photonics. There, both the photonic [1] as well as the excitonic [2] part of the polaritonic mode can be actively utilized to manipulate the overall system topology, yielding significant observations of topological polariton laser oscillation [3–5], spin-momentum locking [6,7], and switching [8,9]. Regarding the experimental implementation, especially atomically thin transition metal dichalcogenide (TMD) monolayers are of great appeal, since excitons therein feature giant light-matter interactions [10–12], and their large binding energies routinely enable the observation of exciton polaritons from cryogenic up to room temperature [13–16].

Despite impressive progress in the technological implementation of tunable and versatile optical microcavities, experiments concerning the topology of photonic or polaritonic modes in microstructured cavity samples were primarily carried out in monolithic implementations. Thus, reconfigurable tuning of these topological modes, and especially substantial *in situ* modification of the emulated potentials, has remained out of experimental reach.

In this Letter, we address this shortcoming, and implement a room temperature polariton system, which is topologically nontrivial, spectrally tunable over an arbitrarily large range, and which can even be reconfigured in terms of the symmetry of the Hamiltonian, allowing us to measure its topological invariants, namely the Zak phase. In our Letter, the topological phenomena arise from the photonic microstructure, and the polariton primarily provides experimental convenience. Our sample structure is schematically depicted in Fig. 1(a). It is composed of two distributed Bragg reflectors (DBRs) of SiO_2/TiO_2 (details can be found in Supplemental Material [17]), which are attached to XYZ nanopositioners with a goniometer and are separated by an air gap. Thus, they form an "open cavity" with full tunability of the air-gap length, relative mirror position, and tilt. The atomically thin WS_2 layer is transferred onto the bottom DBR [see Fig. 1(c)] via scotch tape exfoliation followed by the dry-gel stamping method [18]. The strong coupling regime between excitons in the WS_2 monolayer and the photonic resonance of our cavity is confirmed via momentum resolved photoluminescence spectroscopy (see Supplemental Material [17] for details on the

Published by the American Physical Society under the terms of the Creative Commons Attribution 4.0 International license. Further distribution of this work must maintain attribution to the author(s) and the published article's title, journal citation, and DOI.

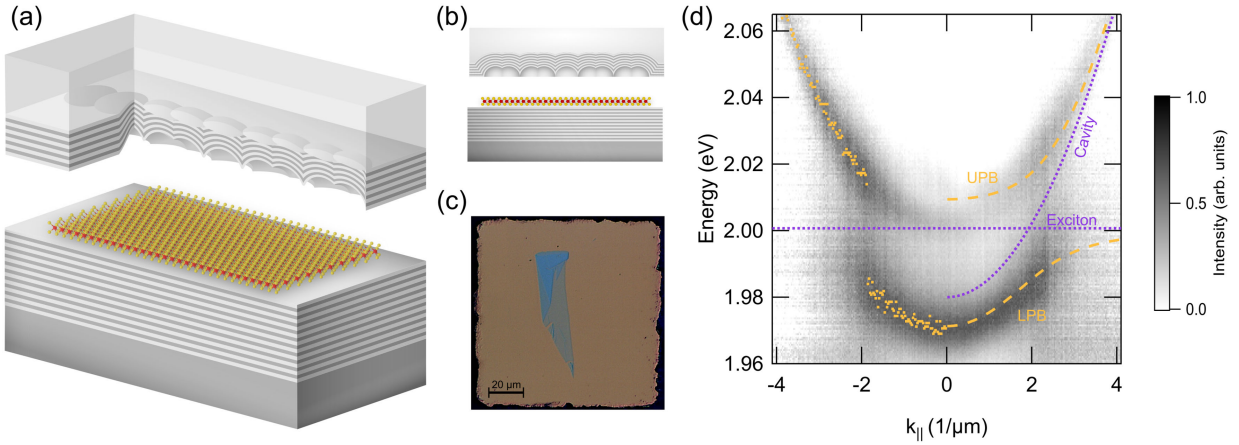


FIG. 1. Open cavity and TMD monolayer sketch and strong coupling conditions. (a) Sketch of the open cavity device, composed of two DBRs surrounding an air gap. The bottom DBR sits on a mesa of 100×100 μm^2. The WS_2 monolayer is placed on top of the bottom DBR, in the maximum of the cavity field. A 1D SSH chain of spherical cap indentations is implemented in the top DBR. Both DBRs can be independently displaced, ensuring full control over spatial and spectral tuning. (b) Side view of the open cavity device sketch to highlight the spherical cap indentations and the central domain boundary. (c) Microscope image of the transferred WS_2 monolayer on top of the DBR mesa. (d) Dispersion relation of the polariton photoluminescence for a $L_{cav} \approx 1.88$ μm, under weak excitation conditions. For negative momentum values ($k_{\parallel} < 0$) the peak location, determined by peak fitting of the polariton modes in the dispersion relation, is indicated by orange dots. As a guide to the eye the excitonic and photonic (upper and lower polariton) modes are represented with violet (orange) lines for positive momentum values ($k_{\parallel} > 0$).

setup design). In Fig. 1(d), we depict an exemplary dispersion relation from our device, which was recorded using nonresonant optical pumping (532 nm wavelength, pump power of $P = 4.7$ μW, and a Gaussian spot size with a FWHM diameter of ≈3.6 μm). The length of the air gap in the cavity was tuned to a distance of ≈1.88 μm. The spectrum is characterized by the two dispersive polariton branches, separated by a Rabi splitting of 32 meV. The spectrum matches the dispersion relation of a coupled oscillator (see Supplemental Material [17]) with a longitudinal resonance mode of the open cavity ($E_C = 1.98$ eV) and the exciton energy of the WS_2 monolayer ($E_X = 2.001$ eV), yielding a negative detuning of $\Delta = E_C - E_X = -21$ meV. As we will show later in this Letter, this detuning can be changed at will via repositioning of the top DBR. As the next step, the confinement of TMD-polaritons is engineered via focused Gallium ion beam (FIB) milling to mechanically shape spherical cap traps of variable diameter, shape, depth, and arrangement [24,25] in the glass carrier which supports the top DBR prior to the deposition of the mirror. In this Letter, we restrict ourselves to a one-dimensional chain of spherical cap indentations [26], which are geometrically arranged in a staggered configuration [see Fig. 1(b)]. Since the intertrap distance dictates the photonic hopping strength, each homogeneous domain of the lattice emulates a potential which is represented by the following expression [27]:

$$H = v\sum_{i=1}^{N}(|a_i\rangle\langle b_i| + \text{H.c.}) + w\sum_{i=1}^{N-1}(|a_{i+1}\rangle\langle b_i| + \text{H.c.}) \quad (1)$$

and which is commonly referred to as the Su-Schrieffer-Heeger model. Here, v and w denote the intra- and intercell hopping amplitudes, respectively. We denote the two sites in the ith unit cell as a_i and b_i. If translational invariance is maintained, the momentum space Hamiltonian can be expressed as

$$H(k) = \begin{bmatrix} 0 & v + we^{-ik} \\ v + we^{+ik} & 0 \end{bmatrix}. \quad (2)$$

Diagonalization of this Hamiltonian yields a dispersion relation of Bloch modes, which form two bands (depicted by "+" and "−") separated by a band gap:

$$\Omega^{\pm}(k) = \pm\sqrt{v^2 + w^2 + 2vw\cos(k)}. \quad (3)$$

This lattice is one of the most widely studied potentials in the field of topology due to its structural simplicity: depending on the unit cell definition (respectively, the sign of $v - w \neq 0$) its topological invariant, the Zak phase, is

$$\gamma_{Zak}^{\pm} = \int_{-\pi}^{+\pi} i\langle u_k|\partial_k|u_k\rangle dk. \quad (4)$$

The integration runs over the full first Brillouin zone and u_k is the cell-periodic part of the underlying Bloch modes. This expression becomes 0 for $v > w$ (topologically trivial) and $\pm\pi$ for $v < w$ (topologically nontrivial). In the system introduced above, we connect two lattices with Zak phases 0 and $\pm\pi$ at a domain boundary, which is expected to give rise to a zero energy mode in the mode spectrum pinned at the center of the gap of width $2|v - w|$. In real space, the mode is localized at

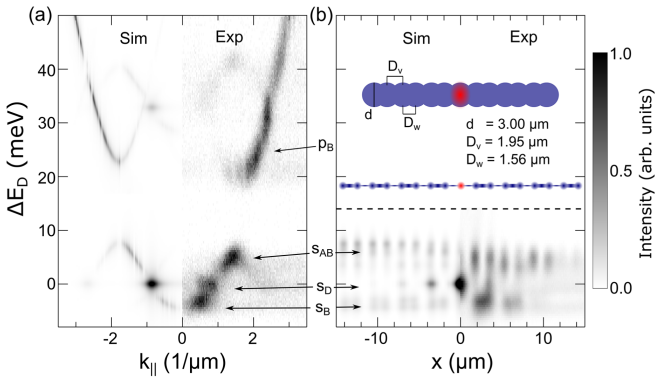


FIG. 2. Real and momentum space properties of SSH lattices. (a) Theoretical dispersion relation showing s and p bands with topologically nontrivial gaps in the s band hosting a localized defect mode (s_D) (left side, $k_\parallel < 0$). Experimental dispersion relation (right side, $k_\parallel > 0$). Energies have been offset by the energy of the defect mode $E_{D,K} = 1.730$ eV in the s band. (b) Top: Schematic drawing of the spherical cap molds of diameter d and staggered center-to-center distance $D_{v,w}$. The defect is located at the center of the chain and the excitation spot is indicated by the red circle. Bottom: spatially resolved spectra of the SSH chain and the localized defect mode ($E_{D,R} = 1.733$ eV) in the s band; ($x < 0$): theoretical calculations, ($x > 0$): experimental emission spectrum. The experimental data represents a small tilt configuration with a tilt gradient of $\mu \approx 0.13$ meV/μm (see Fig. 9 in Supplemental Material [17] for complete experimental data).

the boundary. Its envelope decays exponentially to either side, and it has amplitude contributions on only one sublattice; i.e., it is sublattice polarized. This mode with zero energy is topologically protected from any perturbation in the lattice that does not break chirality of the Hamiltonian. Figure 2 compares the calculated and measured dispersion relation (a), as well as the spectrally resolved real space distribution (b) of the main features in our lattice structure (details on the technique can be found in Supplemental Material [17]). Both, the experimental as well as the calculated spectra are plotted with respect to the energy difference ΔE_D, with the energy of the topological defect state in the s band $E_{D,R} = 1.733$ eV. The simulated as well as the experimentally extracted dispersion relation features a significant spectral gap in the respective bands composed of coupled s-type orbitals (see Supplemental Material Fig. 4 [17]). The size of this gap is directly correlated with the strength of the intra- and intercell hopping parameter v and w. More importantly, a single state is found inside the gap. In real space this mode is exponentially localized in the s band of the lattice and decays with the aforementioned characteristic sublattice polarization [27], which we will discuss later in this Letter in greater detail. The vertical displacement of the microstructured top DBR changes the optical resonance conditions in our system. Consequently, we can control the eigen energies of our optical lattice [26], as well as the energy of the topological mode in the SSH gap over a range approaching 80 meV "on demand," where the TMD polaritons provide a broadband gain medium to populate the radiative modes (see Supplemental Material [17] for further details).

This spectral tuning is essential to build versatile topologically nontrivial photonic devices. In the following, we will focus on the additional ability to modify the tilt between the two mirrors along the lattice via a built-in goniometer. Since the tilt angle between the mirrors is equivalent to continuously changing the cavity resonance and mode energy in real space, it corresponds to a modification of the real-space Hamiltonian of the system as

$$H' = H + \mu \sum_{i=1}^{N} D(i-1)|a_i\rangle\langle a_i| + (iD - D_w)|b_i\rangle\langle b_i| \tag{5}$$

with μ the potential gradient, $D = D_w + D_v$ the unit cell length, and D_w the separation between two neighboring sites belonging to different unit cells i. Since translational invariance is broken, this modification has a large impact on the Hamiltonian. As a first measurable quantity, we inspect the sublattice polarization of the mode in the topological gap of the s band. We define a pseudospin polarization (PSP) for the ith unit cell as

$$PSP_i = \left| \frac{I(b_i) - I(a_i)}{I(b_i) + I(a_i)} \right|, \tag{6}$$

with I the intensity of the emission on a given lattice site. The PSP is related to the total lattice polarization and has thus a strong connection with topological invariants as we will demonstrate below. It has also been measured in waveguide arrays by monitoring the mean displacement of an evolving field distribution [28]. As we induce a potential gradient in the system, we also encounter a striking modification of this PSP. Figure 3(a) shows a series of spatial cross sections extracted at the energy of the defect mode in the s band when systematically sweeping the potential gradient from negative to positive values. At zero gradient [see Fig. 3(b) for the corresponding, spectrally resolved image], we find according to equation (6) a PSP_1 of 0.88 for the first unit cell of the nontrivial domain [see the orange area in Fig. 3(b)]. The PSP drops from 0.88 to 0.75 as we increase the integration window from 1 to 2 unit cells (see Supplemental Material Fig. 12 [17]). PSP_1 as a function of gradient is shown in panel (c). For positive gradients, PSP_1 remains nearly constant i.e., the field of the first unit cell stays localized at the interface. In contrast, for negative gradients, i.e., if the upper dispersive band approaches the energy of the defect mode, PSP_1 is continuously reduced, and eventually approaches 0.5. This asymmetric response with respect to the action of a gradient is due to the spectral position of the interface state, which is closer to the upper than to the lower band as observed in Fig. 3(b). It hints

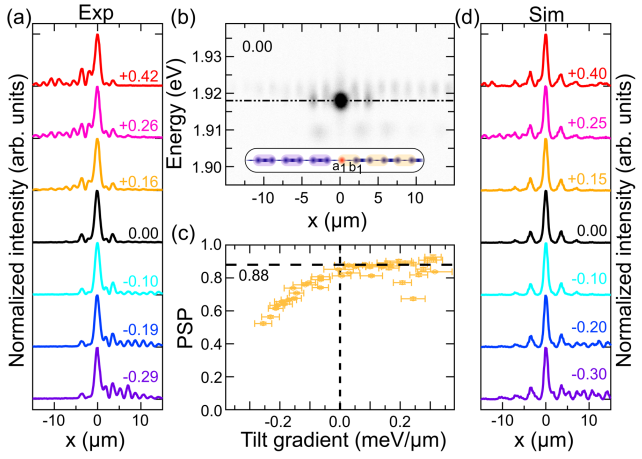


FIG. 3. Actively tuning the topology of polaritons in a lattice. (a) Spatial cross sections extracted from the measured spectra at the energy of the defect mode in the s band for systematically sweeping of the potential gradient. Values of the gradient are indicated in meV/μm. With increasing tilt, the degree of pseudospin polarization (*PSP*) drops and the localization length drastically increases toward the direction where the upper dispersive band allows tunnel coupling. (b) Spatially resolved emission spectrum for zero tilt. The dashed line indicates the spectral position at which cross sections in (a) are extracted. The inset shows the staggered hopping and the definition of unit cells for the trivial (violet) and nontrivial (orange) case in our system. (c) *PSP* of the first unit cell of the nontrivial part as defined in (b) as a function of gradient. The *PSP* is close to 1 and is unperturbed for positive gradients. For negative gradients it gradually decreases due to energetic overlap and tunnel coupling of the localized s band defect mode with the upper dispersive s band. The error bars indicate the standard deviation of the linear regression (see Supplemental Material Fig. 13 [17]). (d) Simulated cross sections extracted at the energy of the defect mode in the s band.

toward an experimental violation of chiral symmetry, most likely due to the presence of long-range coupling. But, as long as inversion symmetry is still present a localized interface state can still exist as demonstrated in Ref. [28]. Figure 3(d) displays the simulated counterpart of panel (a). In close agreement with the experiment, we again observe the reduction in *PSP* and a marked increase in localization length due to the hybridization of the localized mode with the tilted dispersive bands.

Finally, we verify that the tilt applied to our lattice can be directly exploited to measure the topological invariants of our system, which are the Zak phases of the two domains concatenated at the domain boundary. This experiment is conducted at a fixed gradient of $\mu = 0.18$ meV/μm. Figure 4 displays the spatially and spectrally resolved simulation (a) and measurement (b) of our system under these conditions. The upper panel shows the results of simulations within the mean-field model convoluted with a realistic linewidth and spatial mode profile (details can be found in Supplemental Material [17]). We observe that with the applied gradient, the infinitely extended Bloch modes of the lattice transform into spatially localized Wannier-Stark states for both the binding and antibinding s band. A Wannier-Stark ladder exhibits an equidistant energy spectrum [19,20] which still carries information about the topological properties of the lattice with zero gradient. As shown recently for atomic systems [29], the geometric topological phase can be extracted from the energy spectra of these Wannier-Stark states. The energies of the mth Wannier-Stark states $\lambda_m^{\pm}$ are given as a function of the gradient μ and the Zak phase $\gamma_{Zak}^{\pm}$ for the lower "+" and upper "−" bands as

$$\lambda_m^{\pm} = \frac{1}{2\pi}\int_{-\pi}^{+\pi} \Omega^{\pm}(k)dk + \mu D\left(m + \frac{\gamma_{Zak}^{\pm}}{2\pi}\right), \qquad (7)$$

where the periodic lattice has the dispersion relation $\Omega^{\pm}(k)$. Being derived first within the tight-binding model in the limit of small gradient [20], the relation (7) is also valid beyond the tight-binding approach provided that the gradient is small enough and the interband coupling is negligible [see Supplemental Material for a detailed derivation [17]]. It is worth mentioning that the energy separation between Wannier-Stark states is smaller than the line broadening in the system. Nevertheless, these states tend to fuse together forming the intensity spots well visible in the experiment. Our numerical simulations with realistically high losses proved that these non-Hermitian states also respect the lattice symmetries and, thus, satisfy the relation (7) (see Supplemental Material for further details [17]). In Eq. (7) the index m also labels the site, where the intensity spot is localized. Hence, it also demonstrates that the Zak phase is equivalent to a spatial shift resulting in an effective polarization of a nontrivial lattice [30]. We note that this statement is not evident for non-Hermitian systems [31] since the topological invariants and the bulk-edge correspondence were introduced for pure conservative systems. For instance, a strong dependency of the losses from the momenta can lead to the formation of exceptional points which drastically modify the topology [31]. We explicitly show in Supplemental Material [17] by derivation of relation (7) that the losses resulting in the damping of the states (imaginary part) do not change the topology. We also proved this by numerical simulations with different losses and pump spot sizes [see Supplemental Material Fig. 5 [17]]. Consequently, intensity maxima are found at positions

$$X_m^{\pm} = D\left(m + \frac{\gamma_{Zak}^{\pm}}{2\pi}\right) + X_0, \qquad (8)$$

with a constant $X_0 = D_v/2$, if the coordinate origin is chosen at the first site of the nontrivial domain. The application of this formalism to the spatially resolved energy spectrum in the tilted s band of our lattice structure allows us to directly measure the Zak phase difference between the

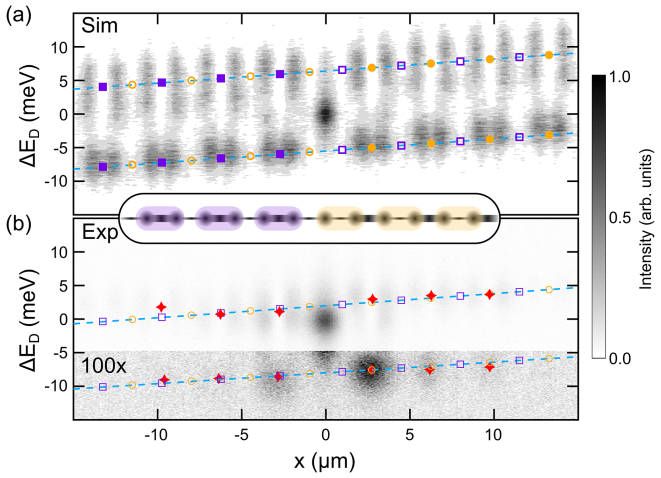


FIG. 4. Zak phase determination. Spatially resolved emission spectrum of the sample for a gradient of $\mu = 0.18$ meV/μm (dashed blue line). (a) Numerical simulation of the energy-resolved photonic components of polariton states in real-space within the mean-field model (see Supplemental Material [17]), assuming a realistic linewidth and spatial mode profile. The violet squares and orange circles depict Wannier-Stark ladders given by the analytical expression [see Eqs. (7) and (8)]. The filled orange circles match the maxima in the topologically nontrivial part of the sample, whereas the filled violet squares match in the trivial domain. (b) Experimental photoluminescence spectra. Red crosses depict the experimental extracted center of gravity of the Wannier-Stark ladder. For better visibility the data below −5 meV was multiplied by a factor of 100. Inset: schematic depiction of the SSH lattice with trivial (violet) and nontrivial (orange) unit cells.

topologically trivial and nontrivial domains from the simulation shown in Fig. 4(a). We calculated the spectrum of the Wannier-Stark states for a fixed gradient, where the dispersion relation $\Omega^{\pm}(k)$ was extracted from the momentum-resolved measurements of the system without gradient [see Fig. 2(a)]. For our definition of unit cells (see inset of Fig. 4) the lattice on the right-hand side from the defect is topologically nontrivial with the Zak phases of $\gamma^{\pm}_{Zak} = \pm\pi$. The violet squares and orange circles in panel (a) depict Wannier-Stark ladders given by the analytical expression from equations (7), (8), calculated for the lower ("+") and upper ("−") bands, respectively. The filled orange circles match the maxima in the topologically nontrivial part of the sample, whereas the filled violet squares match in the trivial domain. This yields a Zak phase difference of $\Delta_{Zak} = \pi$ corresponding to a shift of half of a unit cell between the topological nontrivial and trivial lattice phase for our simulation. In Fig. 4(b) the corresponding experimental results are shown (see Supplemental Material [17]). While, in the topologically nontrivial domain the analytical results from Eqs. (7) and (8) perfectly match the experiment, in the trivial domain we observe a slight offset. Formally, this can be accounted for by a measured Zak phase for the trivial domain of $\gamma_{Trivial} = -0.07\pi$ for the lower s band. We restrict the experimental Zak phase determination to the binding s band since the antibinding states tend to pin to the unperturbed defect states. We justify this slight offset by sample imperfections which can break local inversion and chiral symmetries in the vicinity of the defect. We obtain a Zak phase difference of $\Delta_{Zak} = (1.07 \pm 0.11)\pi$, which is close to the simulated value of $\Delta_{Zak} = \pi$ within error margins.

Our demonstration of an *in situ* tunable topological lattice is of high significance: The large spectral tunability of TMD polaritons at room temperature can directly be exploited in topologically nontrivial devices of enhanced functionality. The topologically nontrivial nature of our tunable defect is of interest for the implementation of a new class of lasers, Bose condensates, and nonlinear light-matter interfaces exploiting geometrical protection of optical modes. Furthermore, electrical injection in similar devices should become feasible with the current state of technology [32]. Last but not least, the feasibility to induce additional potentials and spatial potential gradients will become of high relevance for further studies in particular in the non-linear regime, where linear gradients of cavities are the optical counterpart of applied electrical or gravitational fields. As we furthermore demonstrate, this novel degree of freedom provides a convenient tool to directly measure and analyze topological invariants. Here, we utilized the aforementioned tunability of our system to experimentally extract the Zak phase difference of $\Delta_{Zak} = (1.07 \pm 0.11)\pi$.

Acknowledgments—The authors gratefully acknowledge funding by the State of Lower Saxony. We acknowledge funding by the Lower Saxony ministry for science and education (MWK) within the Landesgraduiertenkolleg "DyNano." Funding by the German Research Society (DFG) within the project SCHN1376 13.1 and 14.2 is acknowledged. O. A. E. and U. P. acknowledge financial support within the DFG project PE 523/20-1. S. T. acknowledges support from DOE-SC0020653 (excitonic characterization of quantum crystals), Applied Materials Inc. (defects testing), and NSF CBET 2330110 (environmental testing). F. E. is supported by the Federal Ministry of Education and Science of Germany under Grant ID 13XP5053A. M. E. acknowledges funding by the University of Oldenburg through a Carl von Ossietzky Young Researchers Fellowship.

[1] L.-H. Wu and X. Hu, Phys. Rev. Lett. **114**, 223901 (2015).
[2] M. Syperek, R. Stühler, A. Consiglio, P. Holewa, P. Wyborski, L. Dusanowski, F. Reis, S. Höfling, R. Thomale, W. Hanke *et al.*, Nat. Commun. **13**, 6313 (2022).
[3] P. St-Jean, V. Goblot, E. Galopin, A. Lemaître, T. Ozawa, L. Le Gratiet, I. Sagnes, J. Bloch, and A. Amo, Nat. Photonics **11**, 651 (2017).

[4] S. Klembt, T. H. Harder, O. A. Egorov, K. Winkler, R. Ge, M. A. Bandres, M. Emmerling, L. Worschech, T. C. H. Liew, M. Segev *et al.*, Nature (London) **562**, 552 (2018).
[5] C. Bennenhei, H. Shan, M. Struve, N. Kunte, F. Eilenberger, J. Ohmer, U. Fischer, S. Schumacher, X. Ma, C. Schneider *et al.*, ACS Photonics **11**, 3046 (2024).
[6] W. Liu, Z. Ji, Y. Wang, G. Modi, M. Hwang, B. Zheng, V. J. Sorger, A. Pan, and R. Agarwal, Science **370**, 6516 (2020).
[7] M. Li, I. Sinev, F. Benimetskiy, T. Ivanova, E. Khestanova, S. Kiriushechkina, A. Vakulenko, S. Guddala, M. Skolnick, V. M. Menon *et al.*, Nat. Commun. **12**, 4425 (2021).
[8] N. Pernet, P. St-Jean, D. D. Solnyshkov, G. Malpuech, N. Carlon Zambon, Q. Fontaine, B. Real, O. Jamadi, A. Lemaître, M. Morassi *et al.*, Nat. Phys. **18**, 678 (2022).
[9] P. Gagel, T. H. Harder, S. Betzold, O. A. Egorov, J. Beierlein, H. Suchomel, M. Emmerling, A. Wolf, U. Peschel, S. Höfling *et al.*, ACS Photonics **9**, 405 (2022).
[10] G. Wang, A. Chernikov, M. M. Glazov, T. F. Heinz, X. Marie, T. Amand, and B. Urbaszek, Rev. Mod. Phys. **90**, 021001 (2018).
[11] K. F. Mak, C. Lee, J. Hone, J. Shan, and T. F. Heinz, Phys. Rev. Lett. **105**, 136805 (2010).
[12] A. Chernikov, T. C. Berkelbach, H. M. Hill, A. Rigosi, Y. Li, B. Aslan, D. R. Reichman, M. S. Hybertsen, and T. F. Heinz, Phys. Rev. Lett. **113**, 076802 (2014).
[13] C. Schneider, M. M. Glazov, T. Korn, S. Höfling, and B. Urbaszek, Nat. Commun. **9**, 2695 (2018).
[14] S. Dufferwiel, S. Schwarz, F. Withers, A. A. P. Trichet, F. Li, M. Sich, O. Del Pozo-Zamudio, C. Clark, A. Nalitov, D. D. Solnyshkov *et al.*, Nat. Commun. **6**, 8579 (2015).
[15] N. Lundt, S. Klembt, E. Cherotchenko, S. Betzold, O. Iff, A. V. Nalitov, M. Klaas, C. P. Dietrich, A. V. Kavokin, S. Höfling *et al.*, Nat. Commun. **7**, 13328 (2016).
[16] Z. Sun, J. Gu, A. Ghazaryan, Z. Shotan, C. R. Considine, M. Dollar, B. Chakraborty, X. Liu, P. Ghaemi, S. Kéna-Cohen *et al.*, Nat. Photonics **11**, 491 (2017).
[17] See Supplemental Material at http://link.aps.org/supplemental/10.1103/qphl-qd37 for more details about the sample, additional experimental data and detailed description of the theoretical model; includes Refs. [18–23].
[18] A. Castellanos-Gomez, M. Buscema, R. Molenaar, V. Singh, L. Janssen, H. S. J. Van Der Zant, and G. A. Steele, 2D Mater. **1**, 011002 (2014).
[19] U. Peschel, T. Pertsch, and F. Lederer, Opt. Lett. **23**, 1701 (1998).
[20] D. N. Maksimov, E. N. Bulgakov, and A. R. Kolovsky, Phys. Rev. A **91**, 053631 (2015).
[21] H. Knopf, N. Lundt, T. Bucher, S. Höfling, S. Tongay, T. Taniguchi, K. Watanabe, I. Staude, U. Schulz, C. Schneider *et al.*, Opt. Mater. Express **9**, 598 (2019).
[22] I. Carusotto and C. Ciuti, Rev. Mod. Phys. **85**, 299 (2013).
[23] A. Amo, J. Lefrère, S. Pigeon, C. Adrados, C. Ciuti, I. Carusotto, R. Houdré, E. Giacobino, and A. Bramati, Nat. Phys. **5**, 805 (2009).
[24] C. Bennenhei, M. Struve, S. Stephan, N. Kunte, V. N. Mitryakhin, F. Eilenberger, J. Ohmer, U. Fischer, M. Silies, C. Schneider *et al.*, Opt. Mater. Express **13**, 2633 (2023).
[25] I. Georgakilas, R. Mirek, D. Urbonas, M. Forster, U. Scherf, R. F. Mahrt, and T. Stöferle, In-situ tunable, room-temperature polariton condensation in individual states of a 1D topological lattice, arXiv:2405.10468.
[26] L. Lackner, M. Dusel, O. A. Egorov, B. Han, H. Knopf, F. Eilenberger, S. Schröder, K. Watanabe, T. Taniguchi, S. Tongay *et al.*, Nat. Commun. **12**, 4933 (2021).
[27] J. K. Asbóth, L. Oroszlány, and A. Pályi, *A Short Course on Topological Insulators*, Lecture Notes in Physics, Vol. 919 (Springer International Publishing, Cham, 2016).
[28] Z.-Q. Jiao, S. Longhi, X.-W. Wang, J. Gao, W.-H. Zhou, Y. Wang, Y.-X. Fu, L. Wang, R.-J. Ren, L.-F. Qiao *et al.*, Phys. Rev. Lett. **127**, 147401 (2021).
[29] R. Mao, X. Xu, J. Wang, C. Xu, G. Qian, H. Cai, S.-Y. Zhu, and D.-W. Wang, Light Sci. Appl. **11**, 291 (2022).
[30] S. Longhi, Opt. Lett. **43**, 4639 (2018).
[31] T. E. Lee, Phys. Rev. Lett. **116**, 133903 (2016).
[32] J. Gu, B. Chakraborty, M. Khatoniar, and V. M. Menon, Nat. Nanotechnol. **14**, 1024 (2019).